Supporting Information

Bimetallic Ag-Au nanoparticles from nanoconfinement: adjusting properties by electrochemical synthesis

Thais Schroeder Rossi,[a] Athanasios A. Papaderakis,[a] Maximilian Jaugstetter,[a] Zaher Jlailati,[a] Miriam Knoke,[a] Pouya Hosseini,[b] Paolo Cignoni,[b] Fengli Yang,[c] Maximilian Gerwin,[a] Oliver Trost,[a] Marius Spallek,[a] Eduardo Ortega,[c] Beatriz Roldán Cueny,[c] Debbie C. Crans,[d] Nancy E. Levinger,[de] Kristina Tschulik[ab]*

[a] Chair of Analytical Chemistry II, Faculty of Chemistry and Biochemistry, Ruhr-Universität Bochum, Universitätsstraße 150, 44801 Bochum, Germany

[b] Max Planck Institute for Sustainable Materials, Max-Planck-Straße 1, 40237 Düsseldorf, Germany

[c] Department of Interface Science, Fritz Haber Institute of the Max Planck Society, Faradayweg 4-6, 14195 Berlin, Germany

[d] Department of Chemistry, Colorado State University, Fort Collins, CO 80523-1872, United States

[e] Department of Electrical and Computer Engineering, Colorado State University, Fort Collins, CO 80523-1373, United States

Corresponding Author

*E-mail: kristina.tschulik@rub.de

Table of Contents

1. Electrodeposition of bimetallic Ag-Au NPs

1.1 Cyclic voltammetry of the binary encapsulated precursors

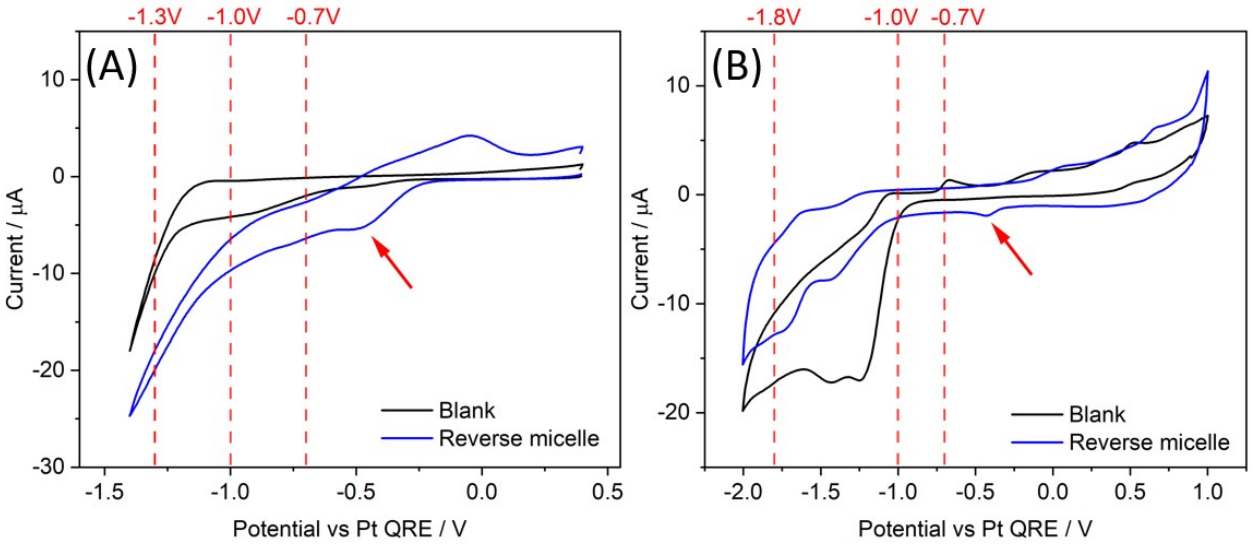

Figure S1. Cyclic voltammograms of bare substrate (black) and substrate with $AgNO_3$+$HAuCl_4$@PS-P2VP reverse micelles dispersed in (A) organic electrolyte ($TBAPF_6$ in DCE + toluene), (B) ionic liquid ($EMIMNTf_2$). Red arrows indicate the reduction peak of precursors. Red dashed lines indicate the potentials used during electrosynthesis. CV plotting convention: IUPAC. WE: HOPG (ZYB grade, 10x10 mm, exposed area = 0.5 cm^2). QRE: Pt wire. CE: Pt gauze. WE compartment is not separated from CE. Applied voltage is not IR corrected. Starting point: 0.4 V and 0.0 V vs Pt QRE for organic electrolyte and ionic liquid, respectively. Direction of the scan: cathodic. Scan rate: 50 mV s^{-1}.

The data presented in Figure S1A shows that upon addition of the encapsulated precursors in the electrolyte, a cathodic wave emerges at ca. −0.25 V followed by an ill-defined peak identified at ca. −0.7 V. The latter is followed by a steep increase in the cathodic current that extends to the cathodic potential limit of the electrolyte. The overall qualitative features of the voltammogram indicate a multiple step deposition process that appears to occur in parallel with the electrolyte decomposition at the most negative potential range. *i.e.*, below ca. −1.0 V.

1.2 Microscopic characterization of the Ag-Au NPs by SEM

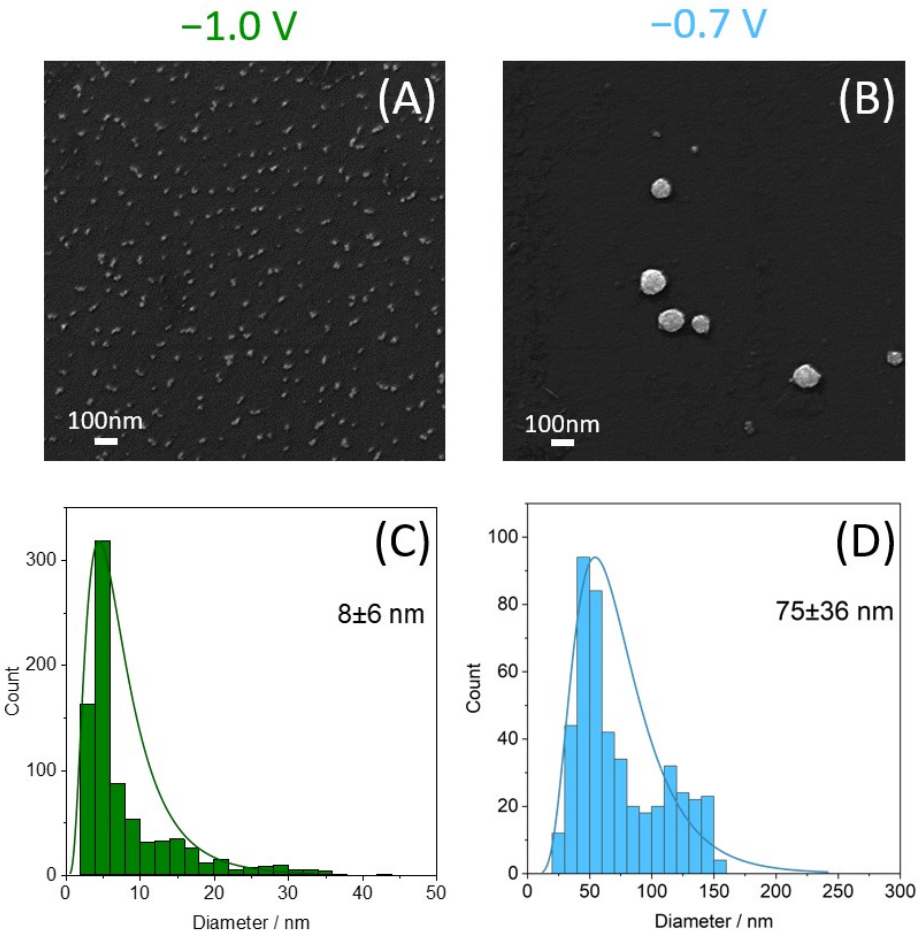

Figure S2. (A,B) SEM image and (C,D) size distribution plot with mean and standard deviation values of Ag-Au NPs synthesized from confined precursors in PS-P2VP reverse micelles in ionic liquid (EMIMNTf$_2$) at −1.0 V, and −0.7 V. Note: mean and standard deviation values were determined from the lognormal fitting parameters μ and σ, as described below.

For size distribution plots fitted with a lognormal distribution, the mean and standard deviation values were determined from the lognormal distribution parameters μ and σ, according to Equations S1 and S2.

$$lognormal\ mean = \exp\left(\mu + \frac{\sigma^2}{2}\right) \quad \text{(S1)}$$

$$lognormal\ standard\ deviation = \sqrt{exp(2\mu + \sigma^2)(\exp(\sigma^2) - 1)} \quad \text{(S2)}$$

An even more negative potential, *i.e.*, −1.8 V, was applied, however this potential did not lead to the formation of NPs on the electrode surface, possibly due to the strong adsorption of the cations on the electrode surface and/or the reductive decomposition of the ionic liquid.[1] A SEM image of electrosynthesis at −1.8 V, with no particles on the electrode is shown in Figure S3.

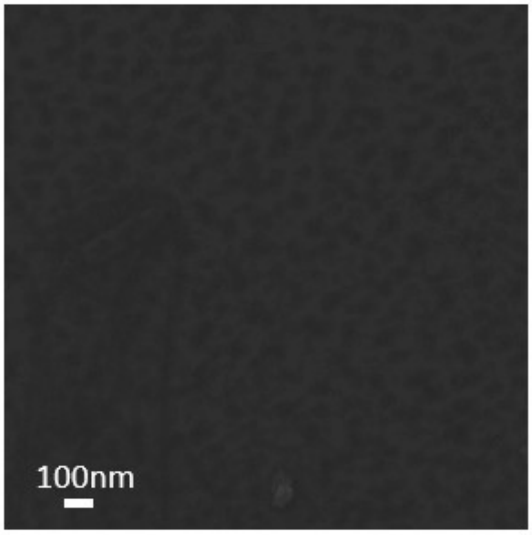

Figure S3. SEM image of an HOPG substrate after Ag-Au NPs electrosynthesis attempt in ionic liquid (EMIMNTf$_2$) at −1.8 V. No NP was observed.

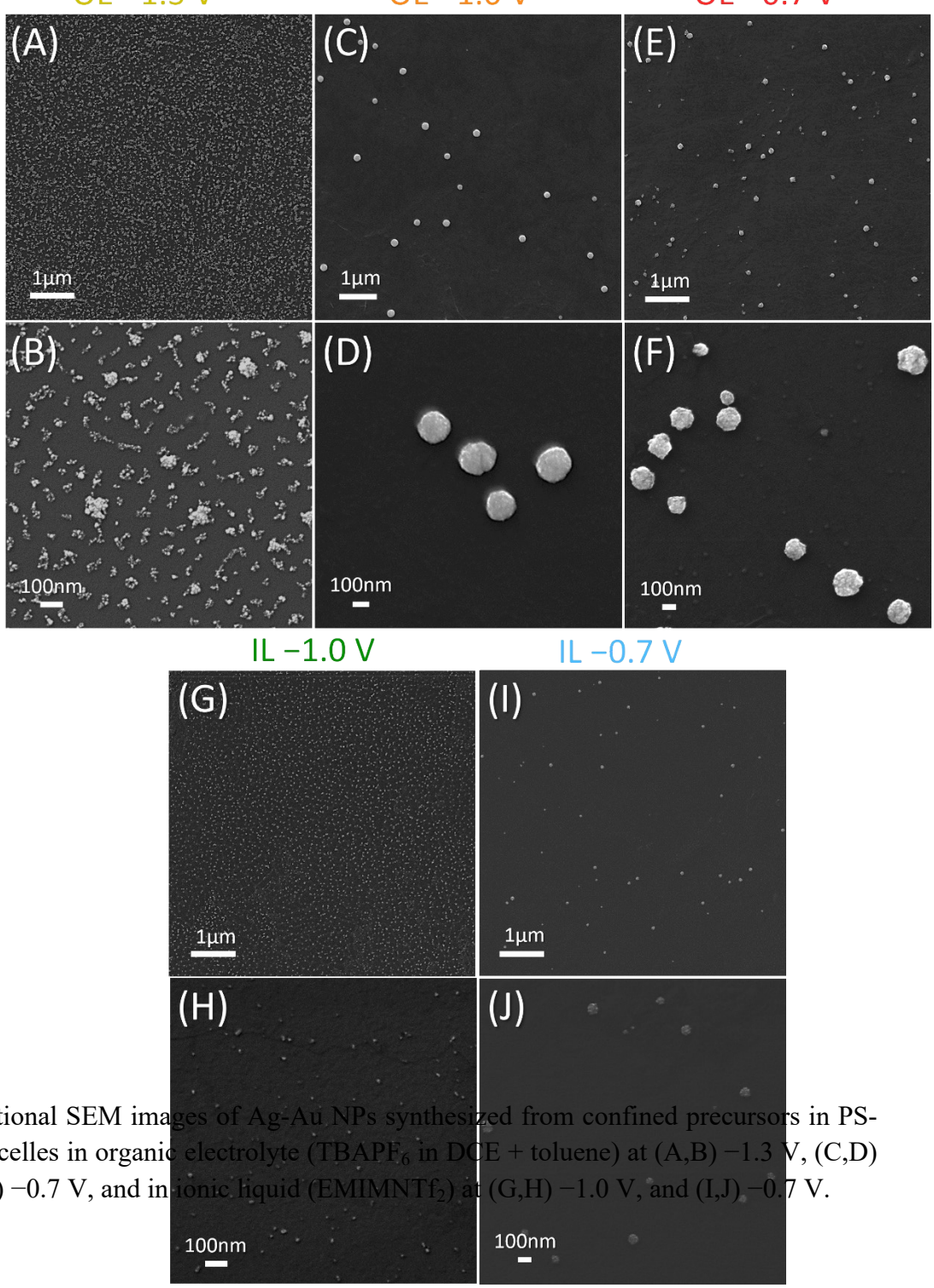

Figure S4. Additional SEM images of Ag-Au NPs synthesized from confined precursors in PS-P2VP reverse micelles in organic electrolyte ($TBAPF_6$ in DCE + toluene) at (A,B) −1.3 V, (C,D) −1.0 V, and (E,F) −0.7 V, and in ionic liquid ($EMIMNTf_2$) at (G,H) −1.0 V, and (I,J) −0.7 V.

1.3 Cyclic voltammetry of the individual encapsulated precursors

In the case of $AgNO_3$ (Figure 2), a shoulder-like reduction peak is seen at ca. −0.6 V followed by a quasi-plateau current region spanning to the cathodic limit of the electrolyte. The peak at ca. −0.6 V and the subsequent plateau-like reduction region can be assigned to the reduction of Ag^+ to metallic Ag, since these features are only detected in the presence of Ag^+. A positive shift in the onset potential of Ag^+ reduction (here defined as the potential corresponding to a current density of ca. 1 μA cm^{-2} relative to the background current, *i.e.*, ca. −0.6 V) of ca. 300 mV is recorded upon successive potential cycles, due to the metal adatom-bulk metal growth following the successful formation of the initial metallic nuclei on the substrate.[2] The anodic peak at ca. −0.07 V, recorded during the reverse scan direction corresponds to Ag stripping in the form of Ag^+. For the Au encapsulated precursor (Figure 2), a cathodic wave at ca. −0.05 V is identified followed by a well-defined reduction peak ca. −1.0 V. The first reduction process can be ascribed to the partial reduction of $^{AuCl_4^-}$ to $^{AuCl_2^-}$, in line with what is reported in the literature for organic solutions[3] as well as acidic aqueous electrolytes.[4] The main cathodic peak can be assigned to the direct $3e^-$ reduction of $^{AuCl_4^-}$ to metallic Au, with a possible minor contribution from the $1e^-$ reduction of $^{AuCl_2^-}$ to Au. During the subsequent potential cycles, the first reduction wave is fully suppressed and a minor negative shift (ca. 35 mV) of the main cathodic peak is observed. Upon sweeping the potential towards the positive direction, the anodic peak seen at ca. +0.07 V can be assigned to the oxidation of Au as a consequence of the presence of water impurities in the electrolyte (the solubility of water in DCE is ca. 80 mM) and/or the adsorption of Cl^-.[3,5]

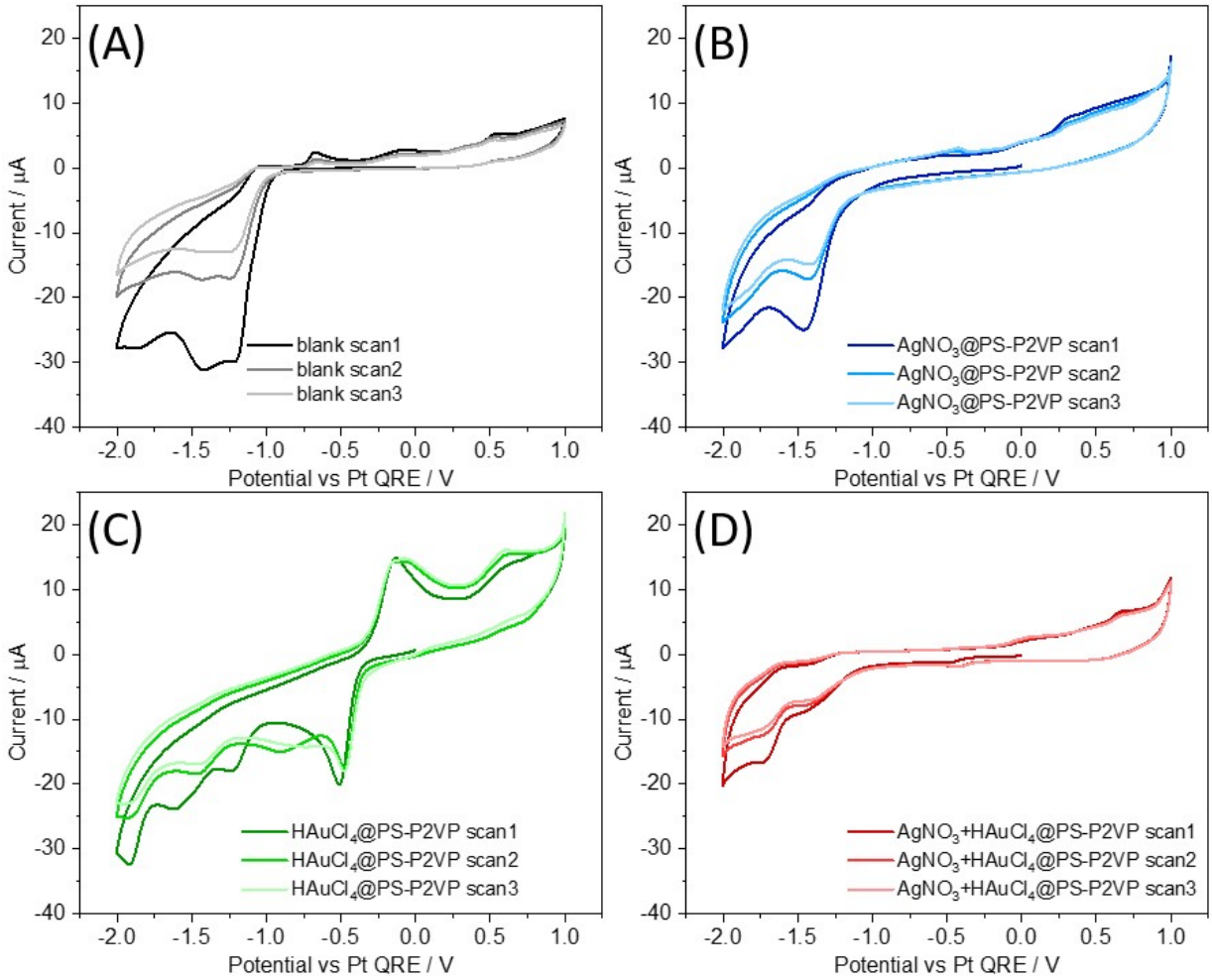

Figure S5. Consecutive cyclic voltammograms of (A) bare substrate, (B) $AgNO_3$@PS-P2VP, (C) $HAuCl_4$@PS-P2VP and (D) $AgNO_3$+$HAuCl_4$@PS-P2VP reverse micelles in ionic liquid ($EMIMNTf_2$). CV plotting convention: IUPAC. WE: HOPG (ZYB grade, 10x10 mm, exposed area = 0.5 cm²). QRE: Pt wire. CE: Pt gauze. WE compartment is not separated from CE. Applied voltage is not IR corrected. Starting point: 0.0 V vs Pt QRE. Direction of the scan: cathodic. Scan rate: 50 mV s^{-1}.

Figure S5C shows the CV scans recorded at HOPG in the presence of gold precursor-loaded reverse micelles. During the first cycle, a well-defined cathodic peak is recorded at ca. −0.5 V accompanied by three successive voltammetric waves. These characteristics are consistent with the well-established two-step reduction of $AuCl_4^-$ reported in ionic liquids.[6] In more detail, the cathodic peak at −0.5 V is assigned to the reduction of $AuCl_4^-$ to $AuCl_2^-$ occurring via the transfer of $2e^-$, while the subsequent peak at ca. −1.22 V corresponds to the deposition of Au through the $1e^-$ reduction of $AuCl_2^-$.[6] The latter peak shifts to less negative potential with potential cycling, due

to the ease of Au-on-Au deposition compared to Au-on-HOPG. The voltammetric waves recorded at more negative potentials are most probably attributed to the strong adsorption of $EMIM^+$ cations on both Au NPs and bare HOPG areas (see also the discussion below), a phenomenon that is reported for various types of cations in ionic liquids.[7–11] By sweeping the potential anodically, two peaks can be identified, which are attributed to the two-step oxidation of Cl^- (produced by the reduction of $AuCl_4^-$) to Cl_2 in line with literature.[5,6] A less complex voltammetric response is seen in the case of the encapsulated $AgNO_3$ precursor (Figure S5B), with a single distinct cathodic peak at ca. −1.46 V, possibly related to the adsorption of $EMIM^+$. No clear features of Ag deposition can be identified, with however an ill-defined anodic peak at ca. −0.4 V (better resolved in the successive potential cycles). Considering that it is not detected in the absence of the precursor (blank, Figure S5A), this might be related to Ag stripping.[12] The apparent difficulty in Ag deposition could be arising from the strong complexation of Ag^+ by the $TFSI^-$ anions.

Elucidation of the processes occurring during electrodeposition from the reverse micelles loaded with individual precursors in $EMIMNTf_2$ allows us to provide mechanistic insights into the overall deposition reaction using the reverse micelles containing both precursors (Figure S5D). To this end, the following reaction pathways are suggested. At −0.7 V and during the first stages of the process, the main reaction taking place is the reduction of $AuCl_4^-$ to $AuCl_2^-$[5,6] as confirmed by the CV scans recorded in the presence of the Au encapsulated precursor (Figure S5). The generated $AuCl_2^-$ is prone to disproportionation via the general reaction scheme (Equation S3):[13,14]

$$3AuCl_2^- \rightleftarrows AuCl_4^- + 2Au^0 + 2Cl^- \qquad \text{(S3)}$$

Note that the rate of the above reaction is enhanced by the presence of Ag^+ ions since the latter complex with the produced Cl^- ions leading to the formation of the insoluble $AgCl_{(s)}$. Precipitation of AgCl shifts the equilibrium in Equation S3 towards the right side and therefore the overall rate of the reaction increases.[13] The first Au nuclei formed by disproportionation of $AuCl_2^-$ gradually promotes the direct Au-on-Au deposition (as evidenced in the positive shift of the relevant peak in the successive potential cycles in Figure S5) and results in the growth of the NPs. At the same time, small amounts of Ag might also be deposited following the metal-on-metal deposition path. At a bias of −1.0 V, a very similar reaction pathway is expected, with Au-on-Au deposition being

further promoted from the relatively early stages of deposition (note that −1.0 V exceeds the peak potential of Au electrodeposition already from the second potential scan in Figure S5).

1.4 Microscopic characterization

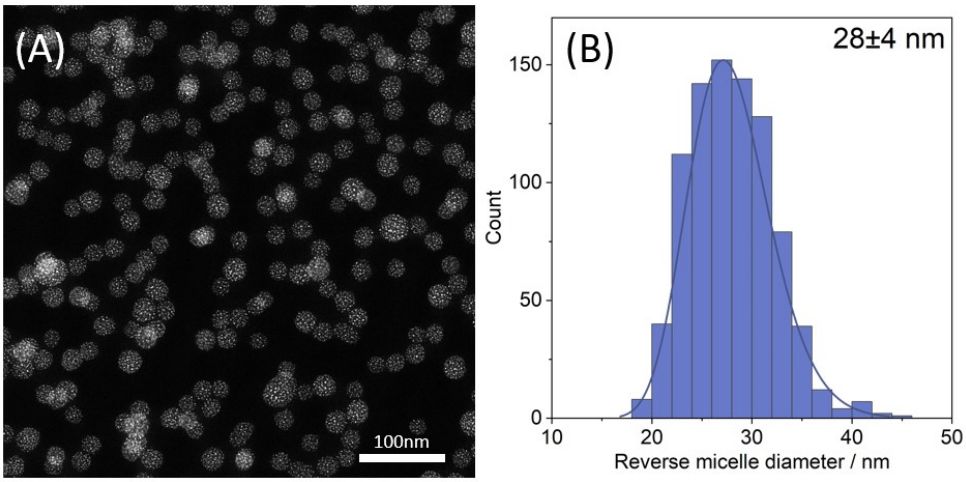

Figure S6. (A) Dark-field STEM image and (B) size distribution plot of $AgNO_3$+$HAuCl_4$@PS-P2VP reverse micelles.

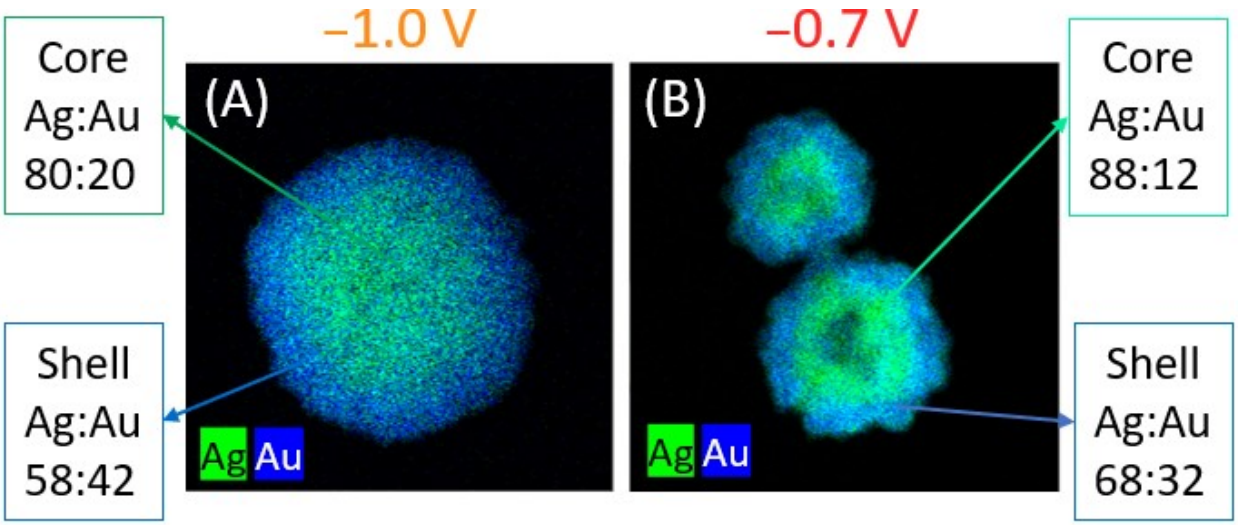

Figure S7. Composition-labelled EDX mapping of the core-shell-like Ag-Au NPs synthesized from confined precursors in PS-P2VP reverse micelles in organic electrolyte ($TBAPF_6$ in DCE + toluene) at (A) −1.0 V, and (B) −0.7 V.

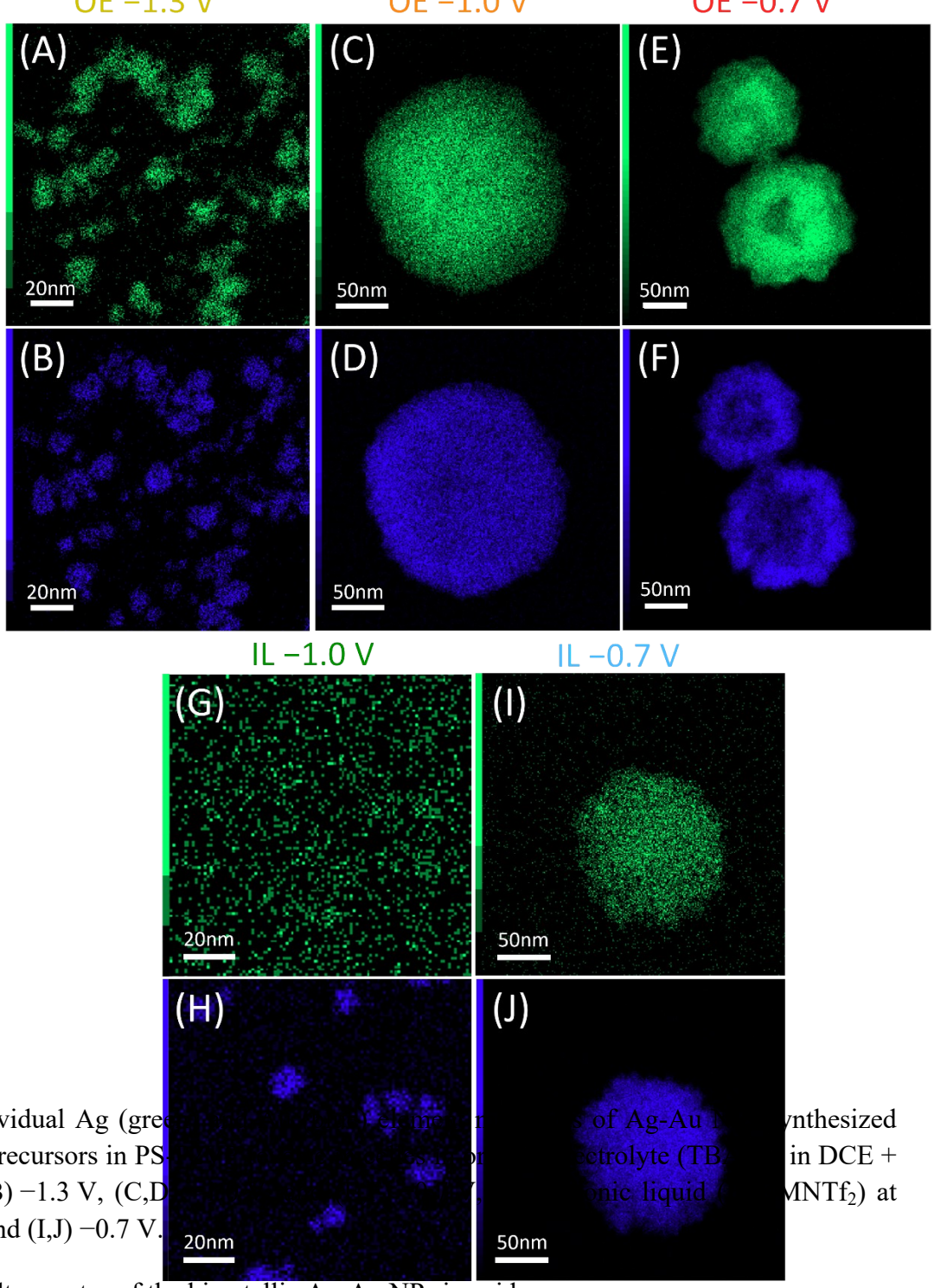

Figure S8. Individual Ag (gre… of Ag-Au … ynthesized from confined precursors in PS… …ctrolyte (TB… in DCE + toluene) at (A,B) −1.3 V, (C,D… …nic liquid … $MNTf_2$) at (G,H) −1.0 V, and (I,J) −0.7 V.

1.5 Stripping voltammetry of the bimetallic Ag-Au NPs in acid

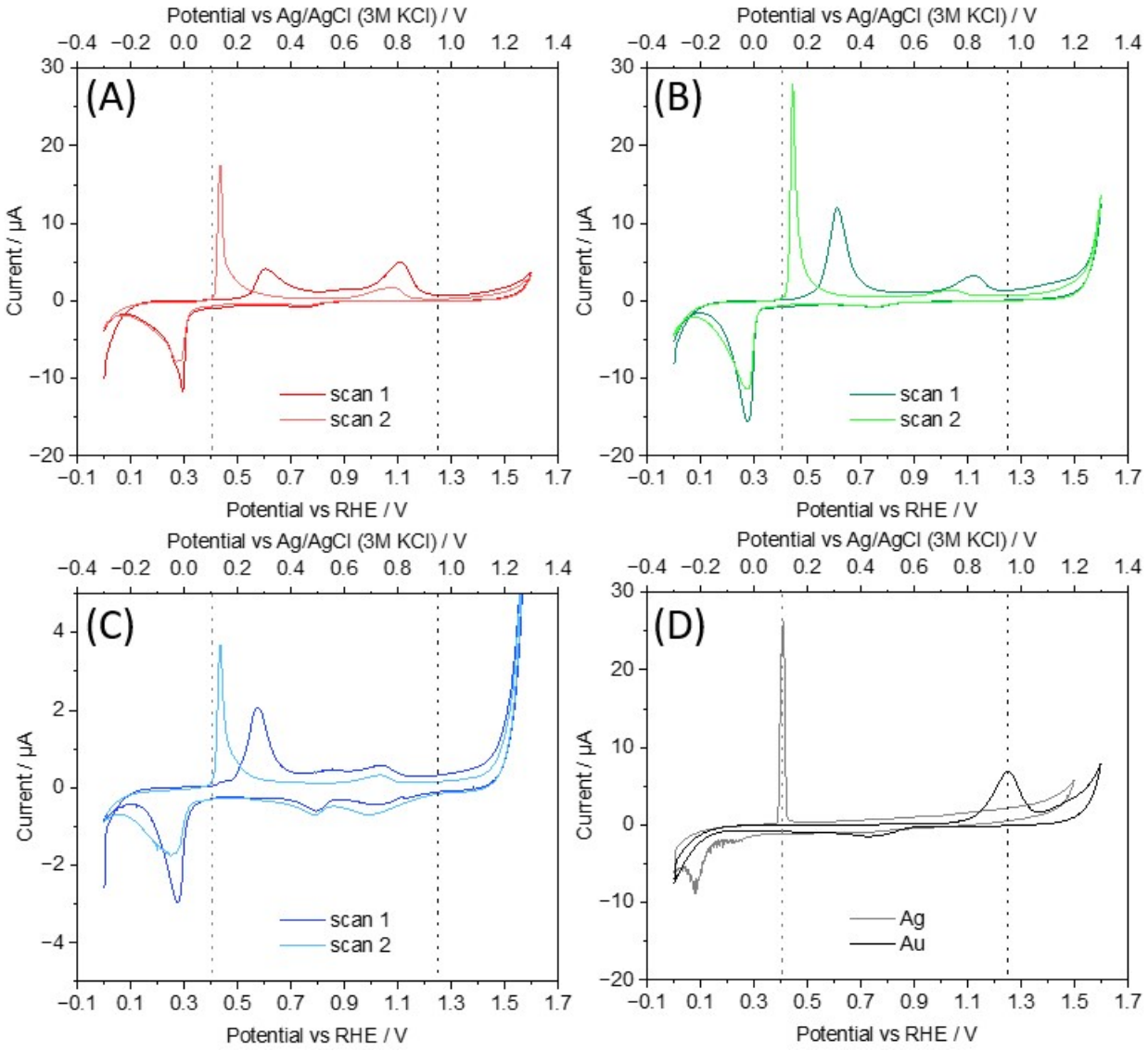

Figure S9. Anodic stripping voltamograms in 0.1 M HCl of Ag-Au NPs synthesized from confined precursors in PS-P2VP reverse micelles in organic electrolyte ($TBAPF_6$ in DCE + toluene) at (A) −1.3 V, (B) −1.0 V, (C) −0.7 V. Dark color: first scan. Light color: second scan. (D) Comparative CVs of commercial Ag NPs (gray) and Au NPs (black). Dotted gray and black lines at the anodic peak potential of Ag NPs and Au NPs, respectively. CV plotting convention: IUPAC. WE: HOPG (ZYB grade, 10x10 mm, exposed area = 0.5 cm²). RE: Ag/AgCl (3 M KCl). CE: carbon rod (⌀= 6 mm). WE compartment is not separated from CE. Applied voltage is not IR corrected. Starting point: −0.3 V vs Ag/AgCl (3 M KCl). Direction of the scan: anodic. Scan rate: 10 mV s^{-1}.

Figure S9 shows anodic peaks that can be assigned to the formation of the sparingly soluble AgCl and the soluble $HAuCl_4$ species, since it is done in chloride solution.[15,16] The first scan, in dark color, shows a broadening and shifting of the Ag (less noble metal) peak, as expected for two metal

mixtures due to the progressive dealloying during the scan towards more positive potentials.[15,17,18] This behavior is observed for Ag-Au NPs formed at all the three investigated applied potentials, which probably happens because the core-shell-type formed at less positive potentials has an alloy shell, therefore the electrolyte can easily reach the Ag-rich core before oxidizing all Au that is in the shell. The second scan, in light color, clearly shows a sharper Ag-related oxidation peak at smaller potential than it was in the first scan, indicating that after the first anodic stripping, Ag and Au do not form the same bimetallic mixture during the subsequent reduction.

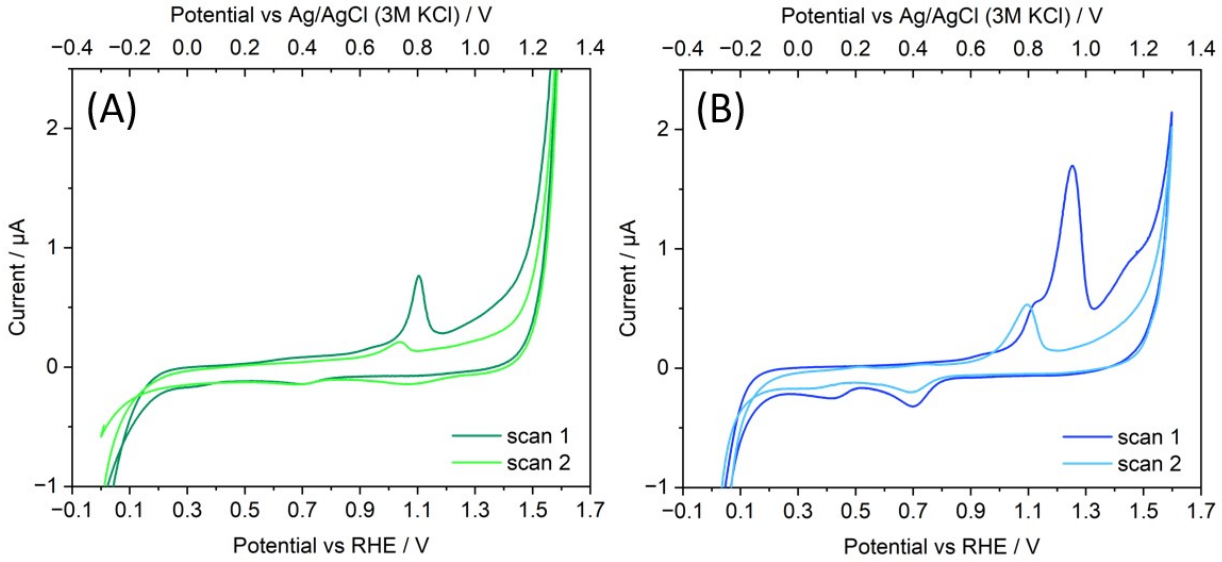

Figure S10. Anodic stripping CVs in 0.1 M HCl of Ag-Au NPs synthesized from confined precursors in PS-P2VP reverse micelles in ionic liquid (EMIMNTf$_2$) at (A) −1.0 V, (B) −0.7 V. Dark color: first scan. Light color: second scan. CV plotting convention: IUPAC. WE: HOPG (ZYB grade, 10x10 mm, exposed area = 0.5 cm^2). RE: Ag/AgCl (3 M KCl). CE: carbon rod (⌀= 6 mm). WE compartment is not separated from CE. Applied voltage is not IR corrected. Starting point: −0.3 V vs Ag/AgCl (3 M KCl). Direction of the scan: anodic. Scan rate: 10 mV s^{-1}.

1.6 Microscopic characterization of Ag-Au NPs from unconfined precursors

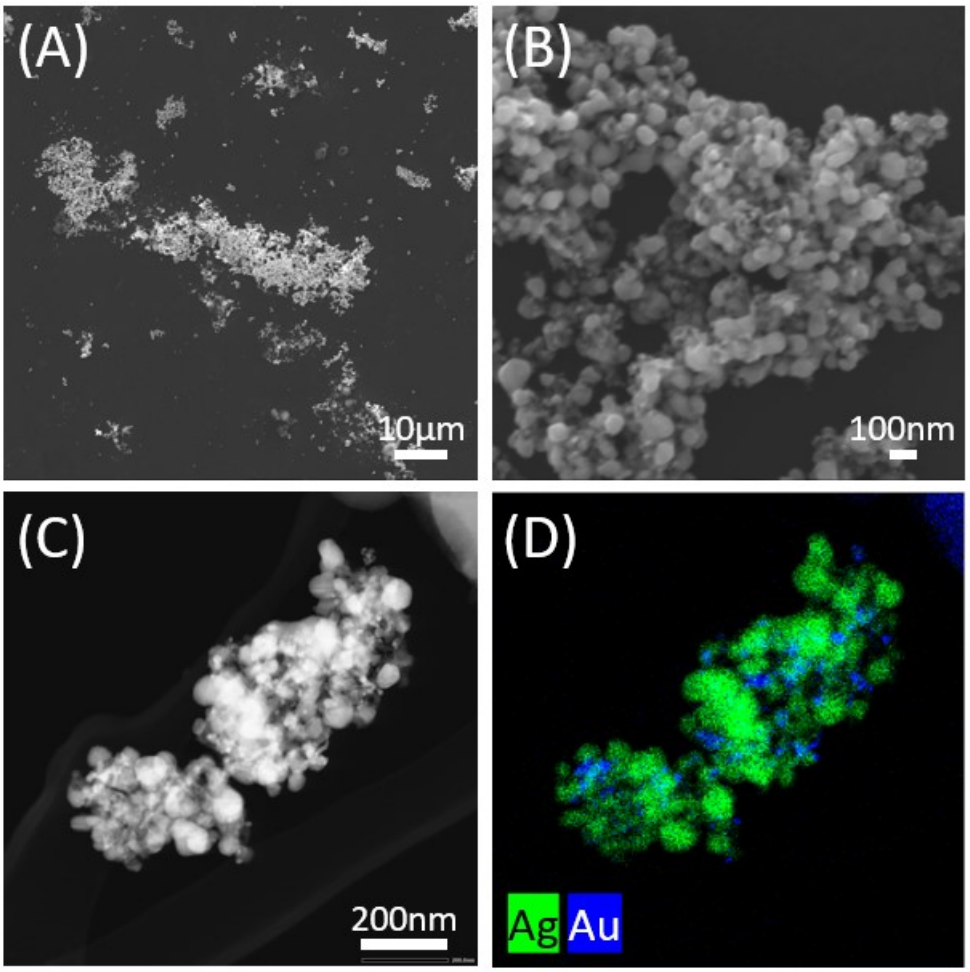

Figure S11. (A,B) SEM images, (C) dark-field STEM image and (D) EDX mapping of Ag-Au NPs synthesized from unconfined precursors in organic electrolyte ($TBAPF_6$ in DCE + toluene) at −1.0 V.

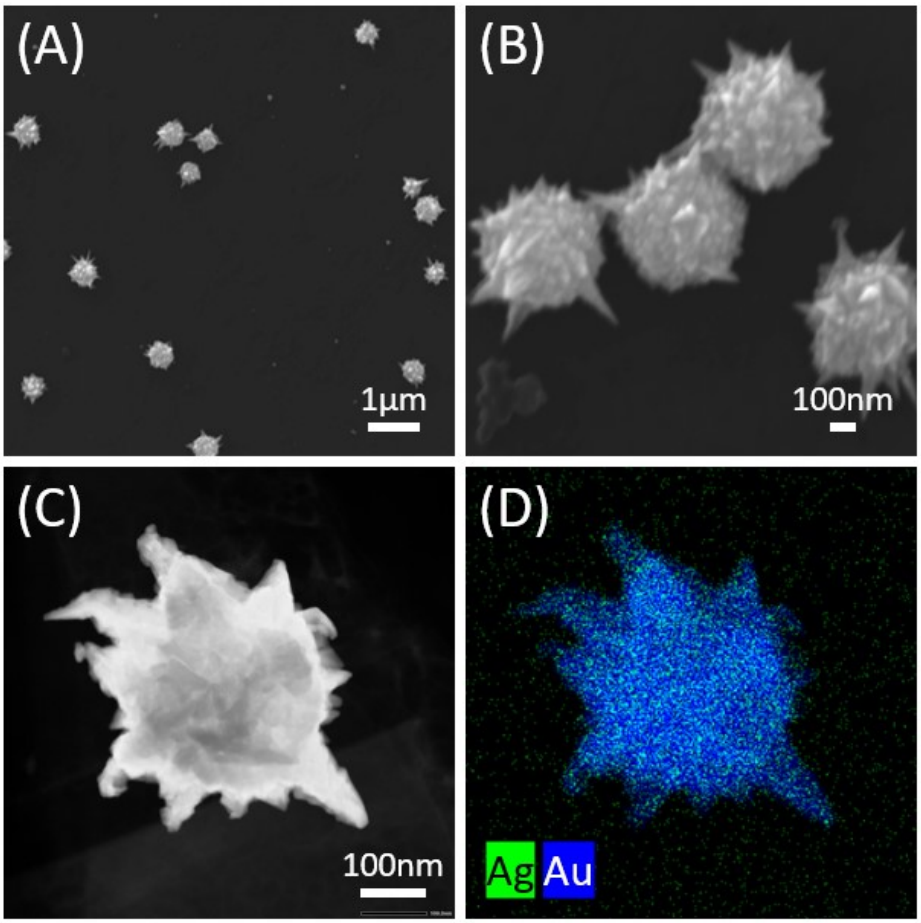

Figure S12. (A,B) SEM images, (C) dark-field STEM image and (D) EDX mapping of Ag-Au particles synthesized from unconfined precursors in ionic liquid (EMIMNTf$_2$) at −1.0 V.

2. Single entity electrochemistry

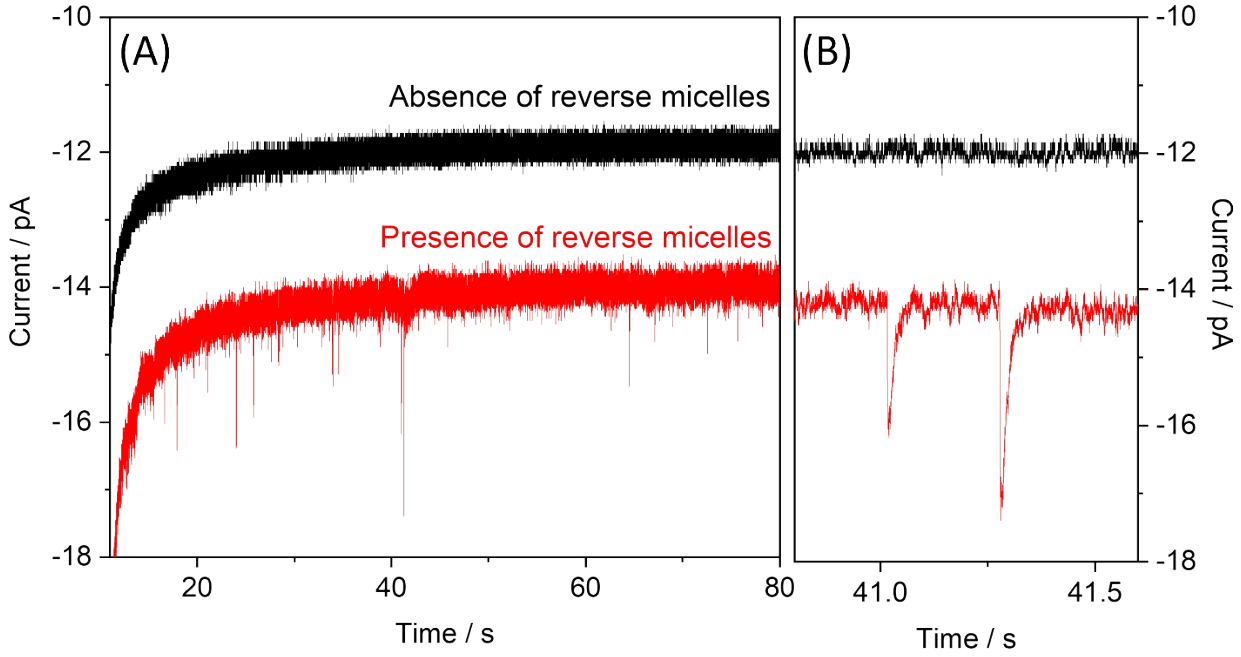

Figure S13. (A) Current-time plot during single entity electrochemical measurements. Spikes are only recorded when reverse micelles are present in the electrolyte. (B) Enlargement of region around 41 s. Electrolyte: ionic liquid ($EMIMNTf_2$). WE: carbon fiber (C, ⌀= 7 µm). QRCE: Pt wire. Potential applied: −1.0 V.

3. X-ray Photoelectron Spectroscopy (XPS)

XPS measurements were conducted directly on the substrate (HOPG). The experiments were carried out using an ultra-high vacuum (UHV) setup equipped with a monochromatic Al Kα X-ray source (energy of 1486.6 eV; anode operated at 14.3 kV and 7.7 mA) and a Scienta Omicron HiPP-3 analyzer. Spectra were recorded in the fixed transmission mode with a pass energy of 500 eV. Charging effects were mitigated by applying a flood gun. Binding energies were calibrated by aligning the graphitic C 1s peak at 284.5 eV. Peak deconvolution was executed using Casa XPS version 2.3.25PR1.0 software.[19]

Additionally, the analysis includes details of the fitting process for the Ag 3d and Au 4f XPS signals (Table S1). A Shirley-type background was employed for the Au 4f. A Linear-type background was employed for the Ag 3d as the signal is weak and overlaps with the decaying background of the C 1s signal of the HOPG substrate. To ensure accuracy, constraints were applied to the peak area ratios and the full width at half-maximum (FWHM (eV)). The FWHM of the Ag $3d_{3/2}$ and the Au $4f_{5/2}$ peaks were constraint to be identical to the Ag $3d_{5/2}$ and Au $4f_{7/2}$ peaks, respectively. Further, in accordance with spin orbit splitting, the relative areas of the Ag $3d_{5/2}$ and Ag $3d_{3/2}$ peaks were constrained to follow the ratio of 3:2. Similarly, the relative areas of the Au $4f_{7/2}$ and Au $4f_{5/2}$ peaks were constrained to the ratio of 5:2. For the Ag $3d_{5/2}$ and Ag $3d_{3/2}$, and Au $4f_{7/2}$ and Au $4f_{5/2}$ peaks, a Lorentzian asymmetric (LA) line shape was adopted. Implementing the asymmetric Lorentzian line shape in Casa involves a parameter denoted as LA(α, β, m), where m is an integer ranging from 0 to 499 that determines the width of the Gaussian used for convolution. Asymmetry in the line shapes was achieved by employing smaller values of α than β, and the overall line shape was slightly modified by convolving it with a Gaussian of width characterized by m.

Table S1. Fitting parameters for the Ag 3d and Au 4f spectra of Ag-Au NPs synthesized from precursors-loaded PS-P2VP reverse micelles in the ionic liquid $EMIMNTf_2$ at −1.0 V: BE: binding energy (eV), LSH: line shape and FWHM: full width at half-maximum (eV).

Species	Name	BE/eV	FWHM/eV	Raw Area	RSF	LSH	Composition At%
Au	$4f_{7/2}$	84.0	1.2	3.34	9.58	LA(1.33, 2.44, 44.69)	90
	$4f_{5/2}$	87.7	1.2	2.50	7.54	LA(1.33, 2.44, 44.69)	
Ag	$3d_{5/2}$	368.0	1.3	0.43	10.66	LA(1.33, 2.44, 44.69)	10
	$3d_{3/2}$	374.0	1.3	0.29	7.38	LA(1.33, 2.44, 44.69)	

To ascertain the composition of surface-near species in the formed Ag-Au NPs, X-ray photoelectron spectroscopy measurements were performed. Figure S14 displays the Ag 3d and Au 4f spectra of the nanoparticles. Due to spin–orbit coupling, the Ag 3d and Au 4f signals exhibit two dominant peaks each, namely $d_{5/2}$ and $d_{3/2}$, and $4f_{7/2}$ and $4f_{5/2}$, respectively. The Au 4f peaks were resolved into two components at binding energies of 84.0 and 87.7 eV, respectively. Similarly, the Ag 3d peaks were also resolved into two components at binding energies of 368.0 and 374.0 eV.

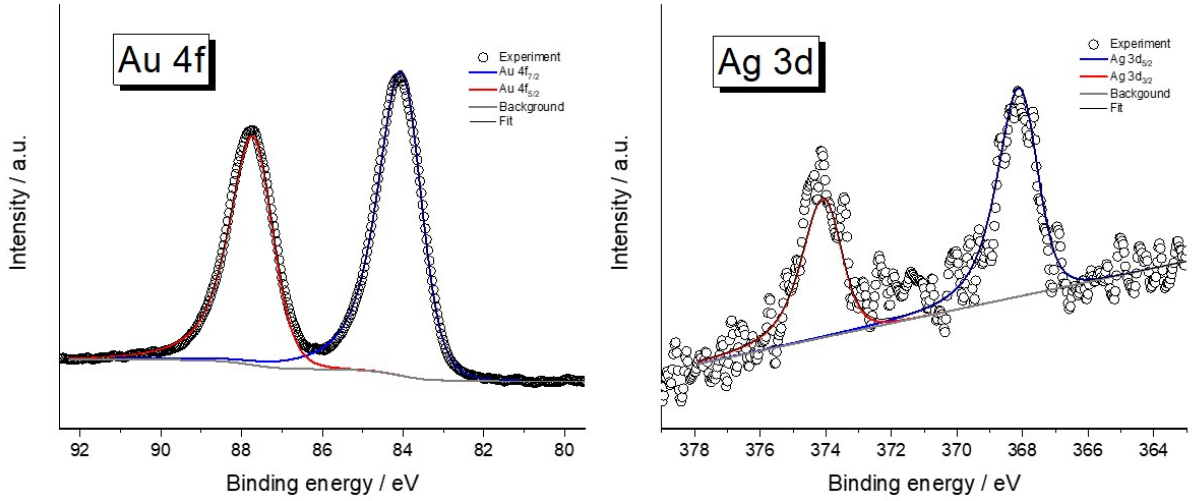

Figure S14. XPS analysis of the Ag 3d and Au 4f spectra of Ag-Au NPs synthesized from precursors-loaded PS-P2VP reverse micelles in the ionic liquid EMIMNTf$_2$ at −1.0 V showing the experimental data points, represented as open circles, while the dark line represents the fit, and the light grey line represents the background.

The elemental compositions obtained from both Energy Dispersive X-ray Spectroscopy (EDX) and surface elemental compositions determined by X-ray photoelectron spectroscopy (XPS) (Table S1) exhibit good agreement. This consistency underscores the high reliability of the synthetic approach.

4. Determination of the electrochemically active surface area (ECSA)

The electrochemically active surface area (ECSA) determination was performed in two steps from the first scan of the anodic stripping CVs in acidic electrolyte media. To illustrate, Figure S15 shows the CV in 0.1 M HCl of Ag-Au NPs synthesized from confined precursors in PS-P2VP reverse micelles in organic electrolyte ($TBAPF_6$ in DCE + toluene) at −1.3 V.

As the first anodic scan might not have completely separated peaks for Ag and Au due to the alloy/core-shell-like structures that are formed, the first step comprises the integration of all the peaks of the first anodic scan (Figure S15A) to determine the charge related to them, which is the charge of Ag and Au combined (Q_{Ag+Au}). On the reverse scan, however, the oxidized species undergo reduction at different potentials, and it is possible to clearly distinguish between the reduction to Au^0 at around 0.45 V and the reduction to Ag^0 at around 0.0 V vs Ag/AgCl (3M KCl) (Figure S15B inset).

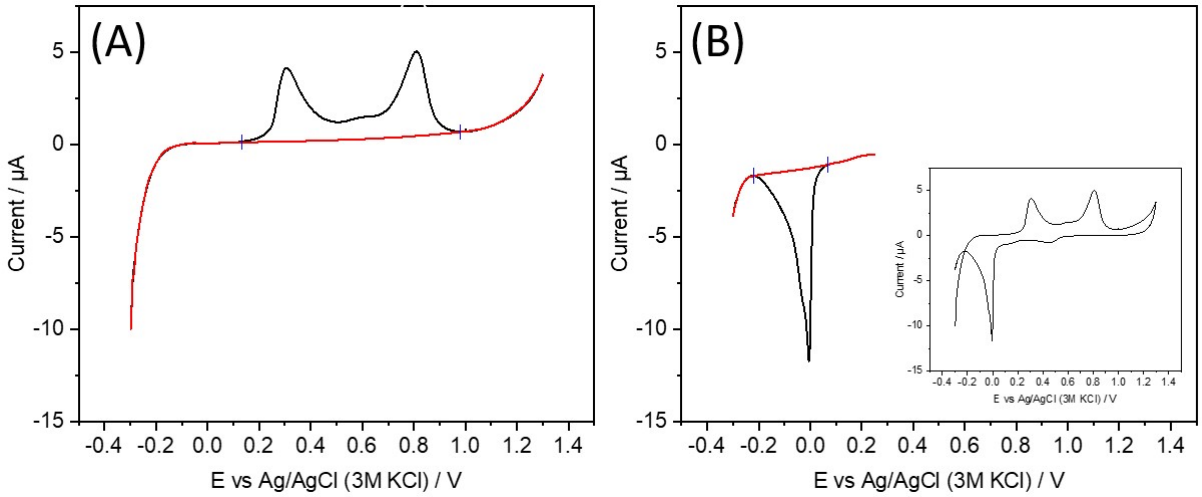

Figure S15. (A) First anodic and (B) part of the cathodic scan of the stripping CV in 0.1 M HCl of Ag-Au NPs synthesized from confined precursors in PS-P2VP reverse micelles in organic electrolyte ($TBAPF_6$ in DCE + toluene) at −1.3 V. Inset: complete first scan. Black curve: data. Red curve: baseline. Blue markers: integration window. CV plotting convention: IUPAC. WE: HOPG (ZYB grade, 10x10 mm, exposed area = 0.5 cm²). RE: Ag/AgCl (3 M KCl). CE: carbon rod (⌀= 6 mm). WE compartment is not separated from CE. Applied voltage is not IR corrected. Starting point: −0.3 V vs Ag/AgCl (3 M KCl). Direction of the scan: anodic. Scan rate: 10 mV s^{-1}.

In HCl, Au oxidizes and can form soluble species, as $AuCl_2^-$ and $AuCl_4^-$, according to Equations S4 and S5.[16] Some of these oxidized species remain close to the electrode surface and are reduced

in the reverse scan, however, some are diffused away from the electrode and, therefore, the gold reduction peak cannot be used as a quantitative measure for the amount of Au that was originally in the NPs.

$$Au + 2Cl^- \rightleftarrows [AuCl_2]^- + e^- \quad \text{(S4)}$$

$$Au + 4Cl^- \rightleftarrows [AuCl_4]^- + 3e^- \quad \text{(S5)}$$

$$Ag + Cl^- \rightleftarrows AgCl + e^- \quad \text{(S6)}$$

On the other hand, Ag oxidizes forming the sparingly soluble species AgCl (Equation S6),[16] which does not diffuse away as it deposits in solid form on the electrode surface. Assuming that all Ag that is oxidized remain on the electrode surface, the silver reduction peak can be then used to determine the total amount of Ag in the original NPs.

Therefore, the second step comprises the integration of the silver reduction peak (Figure S15B) to determine the charge related to silver (Q_{Ag}). By knowing the total charge (Q_{Ag+Au}) and the charge related to silver (Q_{Ag}), the charge related to gold (Q_{Au}) can be determined by Equation S7.

$$Q_{Au} = Q_{Ag+Au} - Q_{Ag} \quad \text{(S7)}$$

By knowing the charge related to each Ag and Au, the volume of Ag and Au can be separately determined by using Faraday's law (Equation S8).

$$Q = znF = z\frac{\rho V}{M}F \quad \text{(S8)}$$

Where Q = charge related to Ag (or Au), z = number of transferred electrons (1 for Ag, 1.9 for Au)[17]; n = mol amount of Ag (or Au); F = Faraday constant; ρ = density of Ag (or Au); V = volume of Ag (or Au); M = molar mass of Ag (or Au).

From the volume of Ag (V_{Ag}) and Au (V_{Au}), the total volume of the NP (V_{total}) can be determined (Equation S9).

$$V_{total} = V_{Ag} + V_{Au} \quad \text{(S9)}$$

Finally, considering the NPs as spheres and the NPs' ECSA as the surface area, we can use the relation between the surface area (A_s) and the volume (V) of a sphere to determine the ECSA (Equations S10 to S12).

$$A_s = 4\pi r^2 \quad \text{(S10)}$$

$$V = \frac{4\pi r^3}{r} \quad \text{(S11)}$$

$$ECSA = \frac{3V}{r} \quad \text{(S12)}$$

Where r = radius of the NPs, taken from SEM and TEM analysis.

5. Nuclear Magnetic Resonance (NMR) Spectroscopy

^{1}H NMR measurements were performed with standard 5 mm NMR tubes filled with 600 µL of the sample using Agilent (Varian) 400MR spectrometer operating at 399.704 MHz. Spectral data were processed using MNova software. The reverse micelle sample was referenced against toluene.

Figure S16 shows the ^{1}H NMR spectra of $AgNO_3$+$HAuCl_4$@PS-P2VP reverse micelles, where peaks assigned to the dispersant medium toluene (at ca. 7.0 and 2.1 ppm) are observed. Peaks at ca. 3.5 and 1.5 ppm are attributable to tetrahydrofuran (THF). In a general reverse micelle environment, water, *i.e.*, the most polar solvent, is entrapped inside the micellar pocket. However, it is also possible to form reverse micelles in the absence of water, using a variety of nonaqueous polar solvents, as glycerol, formamide and methanol.[20] Considering the $AgNO_3$+$HAuCl_4$@PS-P2VP reverse micelles are made in the absence of water and that THF is the most polar solvent present in the system, we assume THF is confined inside the micellar pocket. This assumption is supported by the changes observed in the ^{1}H NMR spectra, where THF peaks of the reverse micelle system are upfield shifted, narrower and with a bigger separation between peaks compared to neat THF, indicating a more structured THF when confined.

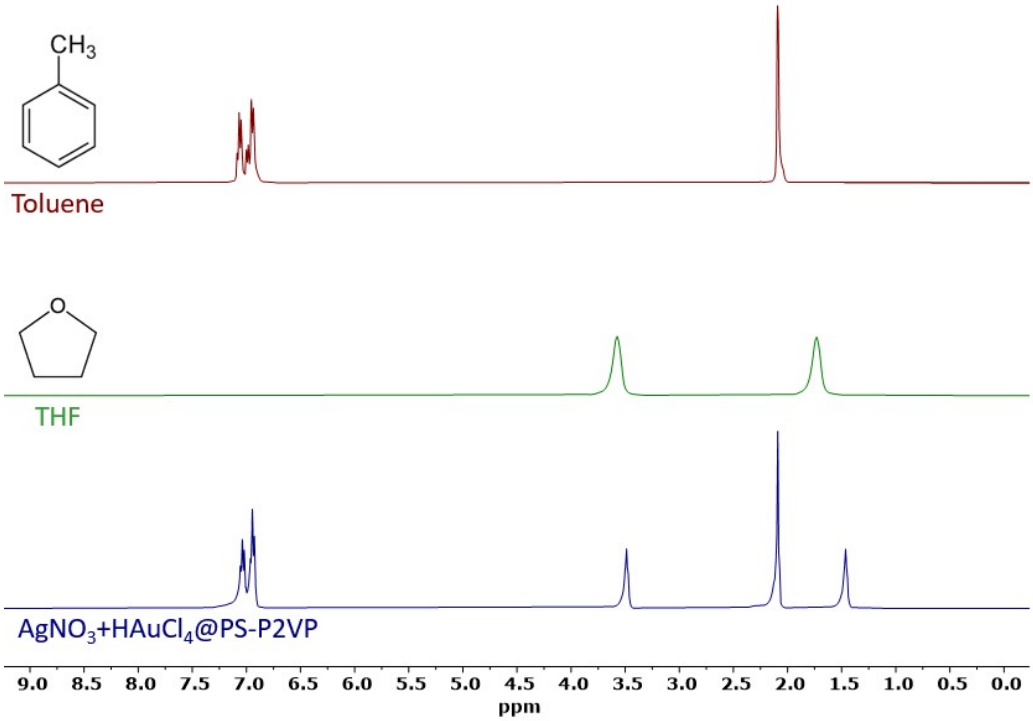

Figure S16. Representative ^{1}H NMR spectra of protonated toluene (burgundy), THF (green) and $AgNO_3$+$HAuCl_4$@PS-P2VP reverse micelles (blue). Inset: chemical structure of toluene and THF. Spectra acquired using Agilent (Varian) 400MR spectrometer operating at 399.704 MHz with standard 5 mm NMR tubes filled with 600 µL of the sample.

6. Inductively Coupled Plasma Mass Spectrometry (ICP-MS)

To identify the amount of Ag and Au leaching from the reverse micelles in toluene, organic electrolyte, and ionic liquid solution, ICP-MS measurements were performed. To prepare the sample for the analysis in toluene, 60.6 µL of the original reverse micelle suspension were diluted with 6 mL of toluene. The samples in organic electrolyte and ionic liquid were prepared analogously to the procedure described for the electrodeposition experiments.

The suspensions were then centrifuged for 1 h at 20000 rcf (Eppendorf 5810 R) to separate intact reverse micelles from the solvent. The supernatant was removed and filtered using a 0.20 µm syringe filter (Chromafil ® PTFE). Due to the incompatibility of the non-polar medium with the ICP-MS device used for the analysis, the leached Au and Ag ions were extracted with an aqueous solution. To increase the accuracy of the measurements, a copper sulphate decahydrate solution (>99%, Sigma Aldrich, the Cu concertation determined by ICP-MS was found 32 µg/L) was used for the extraction, instead of water. Assuming a similar partition coefficient among silver, gold and copper ions, this strategy allows to identify the efficiency of the extraction process and compensating the effect of an incomplete extraction of the analyte ions. For the toluene and organic electrolyte samples, 2 mL of non-polar phase were extracted in 2 steps with a total of 20 mL of aqueous phase. For the ionic electrolyte sample instead, 1 ml of the non-polar phase was extracted in two steps with a total of 10 mL of the aqueous phase. After the extraction the suspensions containing the toluene and dichloroethane were left open for 1 day to allow the complete evaporation of traces of the organic solvents.

The ICP-MS measurements were performed on an Agilent ICP-MS 7900. The copper concentration measured in each sample was similar (33±3 µg/L), indicating a similar efficiency of the extraction process in all the different solutions.

The results obtained were recalculated using the internal standard concentration found in each sample and are summarized in Table S2.

Table S2. Summary of the ICP-MS results (double measurement for each sample), reporting the leached Ag and Au concentrations (c_{Au} and c_{Ag}, respectively) in different solutions obtained by ICP-MS measurements and the maximum concentration of Au and Ag in each sample (calculated considering a 7.5 mM for both precursors in the original reverse micelles suspension and complete extraction).

Solution	c_{Au} /μg L^{-1}	c_{Ag} /μg L^{-1}	$c_{Au,max}$ /μg L^{-1}	$c_{Ag,max}$ /μg L^{-1}	Leached Au / %	Leached Ag / %
Toluene	17±1	1.8±0.1	1477	808	1.2	0.22
Organic electrolyte	1.9±0.1	6.1±0.2	1477	808	0.13	0.75
Ionic liquid	58±1	2.0±0.1	1477	808	3.9	0.25

With the exception of Au in ionic liquid electrolyte (for which around 4% leaching was found) the amount of non-encapsulated Ag and Au in each electrolyte was always around or lower than 1%. Despite the accuracy of the ICP-MS measurements being limited by the complex sample preparation and the lower concentrations involved, we can clearly assume that the vast majority of the precursors is not released from the micelles in the electrolyte solutions. This allows us to clearly indicate that the nanoparticles synthetized with our approach originate directly from the reverse micelles and that contributions from leached ions are negligible.

7. References

1 D. Alwast, J. Schnaidt, K. Hancock, G. Yetis and R. J. Behm, Effect of Li+ and Mg2+ on the Electrochemical Decomposition of the Ionic Liquid 1-Butyl-1-methylpyrrolidinium bis(trifluoromethanesulfonyl)imide and Related Electrolytes, *ChemElectroChem*, 2019, **6**, 3009–3019.

2 D. Pltcher and Walsh F. C., *Metal finishing. In: Industrial Electrochemistry*, Springer, Dordrecht, 1993.

3 L. M. Monzon, F. Byrne and J. Coey, Gold electrodeposition in organic media, *Journal of Electroanalytical Chemistry*, 2011, **657**, 54–60.

4 D. J. Lomax and R. A. Dryfe, Electrodeposition of Au on basal plane graphite and graphene, *Journal of Electroanalytical Chemistry*, 2018, **819**, 374–383.

5 C. Villagrán, C. E. Banks, C. Hardacre and R. G. Compton, Electroanalytical determination of trace chloride in room-temperature ionic liquids, *Analytical chemistry*, 2004, **76**, 1998–2003.

6 L. Aldous, D. S. Silvester, C. Villagrán, W. R. Pitner, R. G. Compton, M. Cristina Lagunas and C. Hardacre, Electrochemical studies of gold and chloride in ionic liquids, *New J. Chem.*, 2006, **30**, 1576–1583.

7 Y.-Z. Su, Y.-C. Fu, J.-W. Yan, Z.-B. Chen and B.-W. Mao, Double layer of Au(100)/ionic liquid interface and its stability in imidazolium-based ionic liquids, *Angewandte Chemie (International ed. in English)*, 2009, **48**, 5148–5151.

8 Y.-Z. Su, J.-W. Yan, M.-G. Li, Z.-X. Xie and Mao, Bing-Wei and Tian, Zhong-Qun, Adsorption of Solvent Cations on Au(111) and Au(100) in Alkylimidazolium-Based Ionic Liquids – Worm-Like versus Micelle-Like Structures, *Zeitschrift für Physikalische Chemie*, 2012, **226**, 979–994.

9 R. Atkin, S. Z. El Abedin, R. Hayes, L. H. S. Gasparotto, N. Borisenko and F. Endres, AFM and STM Studies on the Surface Interaction of [BMP]TFSA and [EMIm]TFSA Ionic Liquids with Au(111), *J. Phys. Chem. C*, 2009, **113**, 13266–13272.

10 J. Yang, F. Hilpert, Y. Qiu, E. Franz, V. Briega-Martos, S. Cherevko, K. Mayrhofer, O. Brummel and J. Libuda, Interactions of the Ionic Liquid [C 2 C 1 Im][DCA] with Au(111) Electrodes: Interplay between Ion Adsorption, Electrode Structure, and Stability, *J. Phys. Chem. C*, 2024, **128**, 2834–2843.

11 M. Jitvisate and J. R. T. Seddon, Direct Measurement of the Differential Capacitance of Solvent-Free and Dilute Ionic Liquids, *The journal of physical chemistry letters*, 2018, **9**, 126–131.

12 M. Deen, C. Shamshoom, A. Gamble, D. Bejan and N. J. Bunce, Electrodeposition of metal cations from the wet ionic liquid [EMIM][TFSI], *Can. J. Chem.*, 2016, **94**, 170–175.

13 S. Eustis and M. A. El-Sayed, Molecular mechanism of the photochemical generation of gold nanoparticles in ethylene glycol: support for the disproportionation mechanism, *The journal of physical chemistry. B*, 2006, **110**, 14014–14019.

14 A. Pearson, A. P. O'Mullane, V. Bansal and S. K. Bhargava, Galvanic replacement mediated transformation of Ag nanospheres into dendritic Au-Ag nanostructures in the ionic liquid BMIMBF4, *Chemical communications (Cambridge, England)*, 2010, **46**, 731–733.

15 P. Cignoni, P. Hosseini, C. Kaiser, O. Trost, D.-R. Nettler, L. Trzebiatowski and K. Tschulik, Validating Electrochemical Active Surface Area Determination of Nanostructured Electrodes: Surface Oxide Reduction on AuPd Nanoparticles, *J. Electrochem. Soc.*, 2023, **170**, 116505.

16 V. Grasmik, C. Rurainsky, K. Loza, M. V. Evers, O. Prymak, M. Heggen, K. Tschulik and M. Epple, Deciphering the Surface Composition and the Internal Structure of Alloyed Silver-Gold Nanoparticles, *Chemistry (Weinheim an der Bergstrasse, Germany)*, 2018, **24**, 9051–9060.
17 E. N. Saw, V. Grasmik, C. Rurainsky, M. Epple and K. Tschulik, Electrochemistry at single bimetallic nanoparticles - using nano impacts for sizing and compositional analysis of individual AgAu alloy nanoparticles, *Faraday discussions*, 2016, **193**, 327–338.
18 B. J. Plowman, B. Sidhureddy, S. V. Sokolov, N. P. Young, A. Chen and R. G. Compton, Electrochemical Behavior of Gold–Silver Alloy Nanoparticles, *ChemElectroChem*, 2016, **3**, 1039–1043.
19 N. Fairley, V. Fernandez, M. Richard-Plouet, C. Guillot-Deudon, J. Walton, E. Smith, D. Flahaut, M. Greiner, M. Biesinger, S. Tougaard, D. Morgan and J. Baltrusaitis, Systematic and collaborative approach to problem solving using X-ray photoelectron spectroscopy, *Applied Surface Science Advances*, 2021, **5**, 100112.
20 N. M. Correa, J. J. Silber, R. E. Riter and N. E. Levinger, Nonaqueous polar solvents in reverse micelle systems, *Chemical reviews*, 2012, **112**, 4569–4602.